

Journal of Thermal Engineering

Web page info: https://jten.yildiz.edu.tr DOI: 10.14744/thermal.0001036



Research Article

Energy and exergy analysis of a novel solar-biomass tri-evaporator multigeneration plant integrated with fuel cell and electrolyzer

Obiora Emeka ANISIJI^{1,2*}, Ikuobase EMOVON², Olusegun David SAMUEL², Fidelis ABAM³

¹Department of Mechanical and Mechatronics Engineering, Federal University Otuoke, Yenagoa, 569101, Nigeria ²Department of Mechanical Engineering, Federal University of Petroleum Resources Effurun, Effurun, 330102, Nigeria ³Department of Mechanical Engineering, University of Calabar, Calabar, 540211, Nigeria

ARTICLE INFO

Article history

Received: 17 February 2025 Accepted: 10 July 2025

Keywords:

Biomass; Exergy; Hydrogen Production; Multigeneration; Solar Energy

ABSTRACT

This study presents the development and thermodynamic assessment of an environmentally benign multigeneration system utilizing solar and biomass resources. The system integrates parabolic trough collectors (PTC), biomass gasification, Organic Rankine Cycle (ORC), Kalina Cycle (KC), vapor absorption system (VAS), electrolyzer, and fuel cell to produce hydrogen, electricity, heating, cooling, and hot water. Thermodynamic analysis is conducted using the first and second laws, focusing on energy and exergy performance. The system is simulated using engineering equation solver (EES), with R245fa and an ammonia-water mixture as working fluids in the ORC and KC, respectively. The proposed system consists of PTC and biomass capacities of 1295 kW and 553.6 kW, respectively, and generates a total power output of 964 kW, including 276.03 kW from the ORC and 145.28 kW from the KC. Post-expansion cooling from the KC provides 129.6 kW at -33.5 °C with 12.15 kW of exergy, while the VAS yields 18.4 kW at 5 °C with 0.24 kW of exergy. The PTC supplies 311.4 kW and 683.8 kW of thermal input to the ORC and KC, respectively. Overall, the system attains energy and exergy efficiencies of 52.2% and 16.14%. The study demonstrates the feasibility and sustainability of integrating solar energy into biomass gasification, supporting its potential for clean energy generation.

Cite this article as: Anisiji OE, Emovon I, Samuel OD, Abam F. Energy and exergy analysis of a novel solar-biomass tri-evaporator multigeneration plant integrated with fuel cell and electrolyzer. J Ther Eng 2025;11(6):1685–1704.

INTRODUCTION

The continuous rise in global energy demand, closely linked to national development, has intensified the urgency to transition from conventional fossil-based power systems to renewable energy solutions [1,2]. This shift is driven by

a combination of factors, including climate change, green-house gas (GHG) emissions, fossil fuel depletion, and volatile energy prices [3]. Renewable energy sources such as solar, wind, biomass, hydropower, and geothermal have emerged as sustainable alternatives, offering the potential to

This paper was recommended for publication in revised form by Editor-in-Chief Ahmet Selim Dalkilic



^{*}Corresponding author.

^{*}E-mail address: anisijieo@fuotuoke.edu.ng

reduce carbon emissions, mitigate environmental degradation, and enhance energy security through resource diversification [4]. In this context, multigeneration systems also referred to as polygeneration systems represent a progressive evolution in energy conversion technologies. Unlike conventional cogeneration or trigeneration systems that typically produce electricity and heating/cooling, multigeneration systems can simultaneously deliver electricity, thermal energy, desalinated water, hydrogen, cooling, and other by-products. These systems enhance overall efficiency by utilizing waste heat and integrating multiple energy outputs within a unified configuration, thereby minimizing fuel consumption and improving sustainability metrics.

Recent global trends underscore the momentum behind renewable energy and hydrogen technologies. By the end of 2024, global concentrated solar power (CSP) capacity reached approximately 6.8 GW, while global bioenergy capacity rose to 150.8 GW, with electrical capacity alone contributing 83.8 GWel across nearly 4,971 operating biomass power plants [5,6]. Electrolytic hydrogen production capacity has surpassed 5 GW, and global hydrogen output is projected to reach 97 million tons in 2024. These figures reflect the expanding role of renewables in supporting clean, integrated energy systems. Solar energy, characterized by its wide availability and scalability, continues to be a cornerstone of the energy transition [7]. Its integration with other renewables, such as biomass, allows for hybrid configurations that offer complementary benefits. Biomass, derived from organic materials like forestry residues and municipal waste, provides a stable energy supply that compensates for the intermittency of solar power [8]. The efficiency of biomass gasification is influenced by factors such as feedstock type, particle size, and operational parameters. Studies have explored related phenomena in solid fuel combustion and transformation, including unburned carbon dynamics [9], briquetting techniques [10], tar characterization [11], grindability indices [12], and grinding energy optimization [13]. Hybrid renewable systems that couple solar and biomass sources offer improved system reliability and resource flexibility. Advanced thermodynamic cycles such as the Organic Rankine Cycle (ORC) and Kalina Cycle (KC) have proven effective for converting low- and medium-temperature heat from these sources into useful energy [14]. ORC systems, in particular, excel in recovering waste heat from industrial and renewable sources, contributing to both energy efficiency and environmental performance [15]. For instance, a solar-biomass hybrid system using Stirling engines and anaerobic digesters was shown to generate 5.6 GWh/year while reducing CO₂ emissions by 7.8 kton/year, with an energy cost of \$0.075/kWh [16].

Numerous studies have modeled and optimized hybrid renewable systems to enhance energy resilience. In Libya, [17] used the System Advisor Model (SAM) to evaluate a PV/wind system with pumped hydro storage, demonstrating reliable load coverage and minimal levelized cost of energy (LCOE). In Gaza, [18] employed HOMER-Pro to

optimize a PV-wind-diesel system for a COVID-19 quarantine center, achieving 100% load reliability and reduced emissions. Similarly, [19] explored a hybrid wind-Stirling dish system for Hurghada, Egypt, and [20] assessed a biogas-based system tailored to the terrain and waste profile of Al-Jabal Al-Gharbi, achieving 86% CO₂ reduction with an LCOE of 3.5 ¢/kWh [21]. Hydrogen integration into multigeneration systems offers further decarbonization potential. As detailed by [22], hydrogen and fuel cell technologies can stabilize renewable energy systems by storing excess electricity and providing clean fuel for multiple end uses. Water electrolysis using surplus renewable energy is central to this approach, particularly in regions with variable solar and wind resources.

Other subsystems, such as Vapour Absorption Systems (VAS), contribute to sustainable energy applications by replacing mechanically intensive vapor compression systems with thermal-energy-driven alternatives [23]. VAS can utilize waste heat from industrial or renewable processes, improving system sustainability for cooling and heating loads. Additionally, Proton Exchange Membrane Fuel Cells (PEMFCs), operating in low (60-80°C) or high (120-200°C) temperature ranges, present efficient pathways for clean electricity generation from hydrogen [24]. Multigeneration systems have already been deployed in industrial sectors such as pulp and paper, salt, and district heating, particularly in Europe. For example, Finland and Sweden have pioneered the use of forest residues and roundwood for electricity and heat generation [25]. Meanwhile, several researchers have proposed novel configurations integrating multiple renewable inputs and thermodynamic cycles. [26] developed a solar-biomass-wind polygeneration system incorporating gasification, CO2 capture, ammonia synthesis, and ORC technologies. [27-30] examined variations of solar-based multigeneration systems utilizing combinations of Kalina cycles, Brayton cycles, supercritical CO2 cycles, and desalination technologies. Recent innovations include [31]'s solar tower system that integrates Brayton, transcritical, and organic Rankine cycles with PEM electrolysis and ammonia synthesis. The system produced 4938 kW of net power and demonstrated notable hydrogen and ammonia outputs with energy and exergy efficiencies of 26.71% and 26.16%, respectively. [32] reported a CSP-based system producing 3.62 MW of power and 0.0072 kg/s of hydrogen. Similarly, [33] evaluated a solar-geothermal hybrid system generating 56.6 kg/day of hydrogen and 1.47 kg/s of freshwater with enhanced power generation from thermoelectric integration. [34] compared basic and regenerative ORC cycles coupled with reverse osmosis, highlighting performance sensitivity to turbine and condenser pressure settings.

The following evaluation objectives were taken into consideration while conducting the above thorough literature review: the architecture of the multigeneration system, the system's primary energy resources and how they are converted, the effective utilization of energy sources for

each subsystem, the method of producing hydrogen, the decarbonization of power production, the system, and its primary end products. It is found that a multigeneration energy system powered by a combination of biomass and solar energy sources with PTC system running on a hybrid nanofluid (MWCNT-Al₂O₃ / therminol VP1), incorporating and utilising the tri-evaporator system has not been investigated by integrating a unique ORC system combined with Kalina Cycle, Vapour absorption system, Proton exchange membrane, and a fuel cell, using minimal energy of the configured system to generate Electricity, Heating, Cooling, hot water, and Hydrogen. Furthermore, the performance of linked subsystems in such a multigeneration system must be investigated under various operational conditions. It is anticipated that these systems will open up several new possibilities for using biomass and solar energy sources.

Inspired by these gaps in the literature, this study proposes an integrated energy system that generates clean energy from renewable sources. A key innovation lies in the use of a single working fluid to drive three interconnected subsystems. By strategically bleeding the fluid during turbine expansion, the same medium is repurposed for cooling production. This integrated design shortens the thermodynamic process path, reduces system complexity, and minimizes the number of components required. As a result, it enhances overall performance, boosts energy utilization, and achieves a higher cooling-to-power ratio—an especially noteworthy aspect of this study. Furthermore, the paper develops models for an innovative cycle featuring a tri-evaporator system. This includes a conventional evaporator in the vapour absorption system (VAS) and unconventional evaporators in both the organic Rankine cycle (ORC) and Kalina cycle (KC) subsystems. The tri-evaporator configuration provides numerous benefits, such as increased cooling capacity, improved heat recovery, enhanced flexibility, reduced temperature differentials, greater system reliability, better heat transfer, and improved overall energy efficiency. By enabling heat recovery from multiple sources, minimizing thermal stress, and offering operational redundancy, this configuration represents a significant advancement in integrated energy systems.

The objectives of this research include the development of a new renewable energy-based integrated system capable of producing various utilities. To achieve this, the study involves a thorough investigation using thermodynamic balance equations for each system component, analyzing how state properties and varying operating conditions impact individual subunit performance as well as the system's overall performance.

In this paper, we further present a comprehensive analysis starting with the system description, including detailed insights into each component such as the parabolic trough collector (PTC), Kalina cycle (KC), organic Rankine cycle (ORC), vapour absorption system (VAS), proton exchange membrane (PEM) electrolyzer, biomass combustor, and a

fuel cell. Then the energy and exergy analyses, are discussed providing balance equations for different components to evaluate performance.

MATERIALS AND METHODS

Materials

The National Aeronautics and Space Administration (NASA) database provided daily meteorological data on solar irradiation for the Otuoke University community for 15 years. Furthermore, the biomass is woody waste of different wood species from tropical hardwood timber harvesting/logging in Otuoke. The average data served as the foundation for selecting simulation data for the planned multigenerational system and its components. Furthermore, the system modelling was conducted using Engineering Equation Solver (EES), and secondary data was sourced from publicly available literature and scientific sources.

System Assumptions

The whole system operated at steady state with negligible changes in potential and kinetic exergy. The ambient temperature and pressure at inlet to the turbine were taken as 25°C and 1.013 bar, unless otherwise indicated during parametric analysis. The remainder of the input data for simulation across the entire plant is summarised and presented in Table 9.

System Description

The proposed multigeneration architecture is shown in Figure 1. The system overview shows that the parabolic trough collector (PTC), powered by the sun, is the integrated energy system's primary energy source, the Kalina cycle (KC) provides power and cooling, the organic Rankine cycle (ORC) also provides power and cooling, the vapour absorption system (VAS) provides cooling, a proton exchange membrane (PEM) electrolyzer for hydrogen production powered by a biomass combustor and a fuel cell powered by hydrogen from the PEM electrolyzer. Starting with the PTC, a hybrid Nanofluid (Multi-walled carbon nanotube and Aluminium dioxide (MWCNT -Al₂O₃ / therminol-VPI) which is the heat transfer fluid of the subsystem, enters the solar collector as stream 54, and its energy is raised. The superheated exiting stream 52 from the PTC flows first into the vapour generator (VG for KC) for the Kalina cycle and transfers some of its thermal energy to the KC working fluid. Exiting as stream 53, it enters the vapour generator of the organic Rankine cycle (VG for ORC) and secondly transfers some more of its heat energy to the ORC working fluid. The hybrid Nano fluid returns to its initial state 54, and the cycle goes on continuously. Superheated steam-ammonia (NH₃-H₂O), the working fluid (stream 1) of the Kalina cycle leaves the vapour generator (VG for KC) and enters a separator (S1) and flashes into stream 2 and stream 3. Stream 2 is a

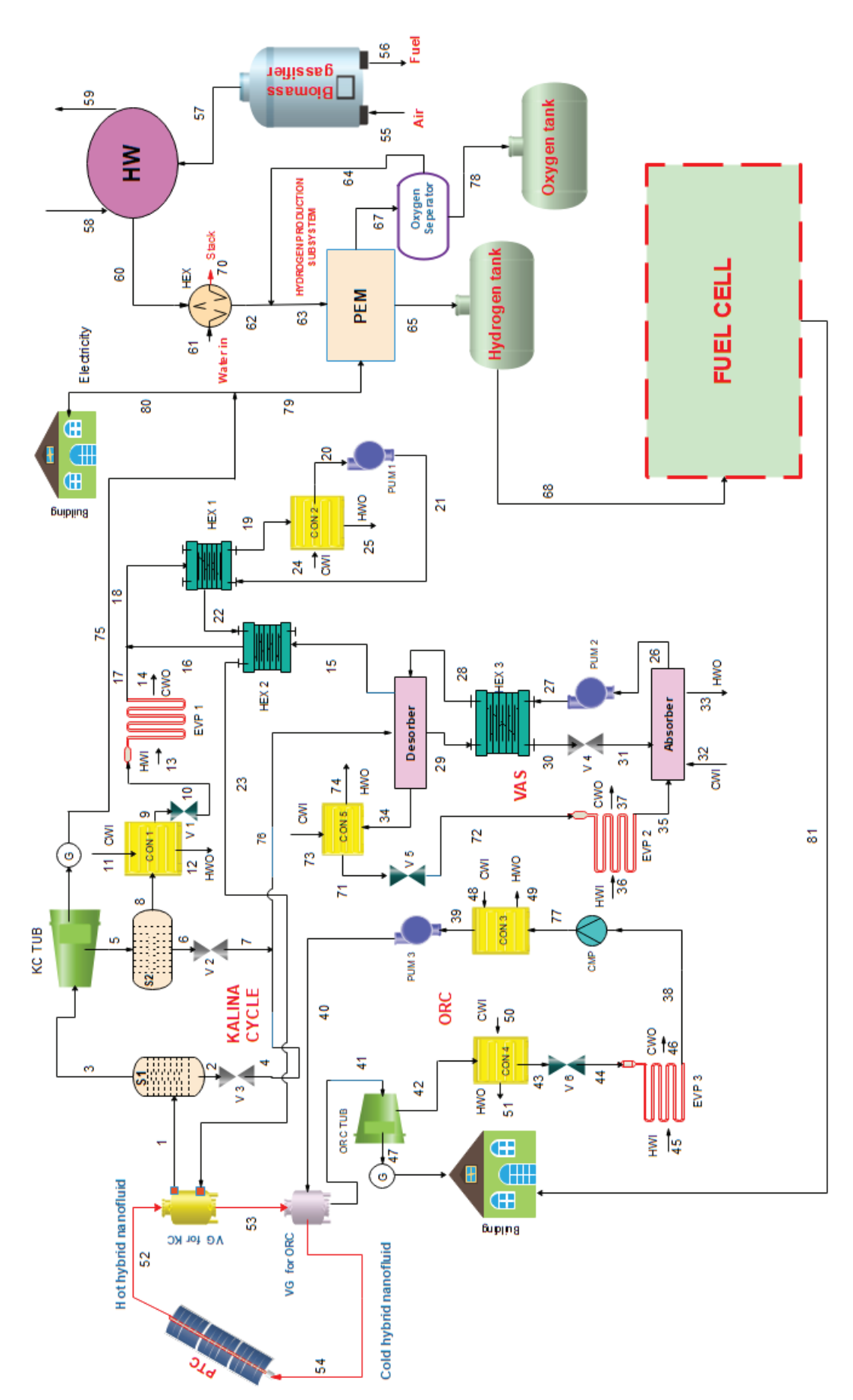


Figure 1. The proposed solar-biomass-based multigeneration system.

high-pressure, temperature condensate that flows through a throttling valve resulting in low-pressure stream 4. Stream 3, which is a high temperature and pressure steam ammonia passes and expands through the Kalina turbine converting some thermal energy into Mechanical shaft work that drives an alternator to generate electricity. The expanded vapour (stream 5) flows into a separator (S2) and splits into a lower-pressure condensate (stream 6), and another lower-pressure and temperature vapour (stream 8). Stream 6 is throttled into lower pressure stream 7 which mixing uniformly with stream 4 results in stream 76. Stream 8 is condensed into a lower temperature stream 9 by a high-pressure condenser (CON1), and then throttled into a lower pressure stream 10, it gains heat by the cooling process in the evaporator (EVP1), exits as stream 17 and mixes uniformly with stream 16 to yield stream 18. This transfers its heat energy in the heat exchanger (HEX1), exiting as stream 19, it further loses its heat in the low-pressure condenser (CON 2) and exits as stream 20, whose pressure is increased in the pump (PUM 1) to become stream 21 that gains heat in HEX1 into stream 22, and further gains more heat in the heat exchanger (HEX2) to exit as stream 23 which returns to the VG for KC and the cycle continues in that order. The working fluid (R245fa) of the organic Rankine cycle (ORC) subsystem receives its heat energy from VG for ORC and then flows as stream 41 to expand in the turbine, converting some of its heat energy to shaft work that drives an alternator to produce electric power. Exiting as stream 42 and entering into the high-pressure condenser (CON4), it loses some of its energy and exits as stream 43, whose pressure is further lowered when throttled to stream 44. It gains heat energy through the cooling process in the evaporator (EVP3) and leaves as stream 38, which is compressed by the compressor (CMP) into stream 77. Stream 77 flows into the low-pressure condenser (CON3), releasing some of its heat energy and flows out as a low-temperature, low-pressure stream 39, which is pumped by a pump (PUM3) back to VG for ORC as stream 40. This cycle continues in this manner. The ammonia-water fluid fraction (stream 76) from the Kalina cycle separators (S1 & S2) transfers heat to the Lithium Bromide water (LiBr-H₂O) solution inside the desorber and exits as stream 15. When the weak LiBr-H₂O solution (stream 28) is heated, a portion of the water absorbed by the LiBr is released as vapour (stream 34). Due to the removal of water from the remaining solution, it becomes more concentrated (stream 29). The water vapour coming from the generator/desorber is then condensed (CON 5) to a saturated liquid state in a condenser (stream 34 to stream 71), where the heat rejected is utilized for space heating/hot water production. The condensed liquid is then throttled to a lower pressure. This pressure is determined by setting the evaporator temperature to be the saturation temperature and determining the corresponding saturation pressure. After throttling, the refrigerant is in the saturated liquid-vapour state

(stream 72). Afterwards, the refrigerant is passed through the evaporator, where the refrigerant absorbs heat from the space being cooled/air-conditioned. After the evaporator, the refrigerant is sent to the absorber (stream 35). The strong solution exiting from the desorber is passed through a heat exchanger (HEX3) and recovers some heat (stream 29 to stream 30) that was provided to the solution in the desorber. And then, the heat is transferred to the incoming weak solution (stream 27 to stream 28). After the heat exchanger, the strong solution is then throttled to a lower pressure in the absorber (stream 31). The strong solution (stream 31) coming into the absorber is cooled by rejecting some heat into the atmosphere. The lower temperature of the solution increases its capability to absorb water vapour, and therefore, the vapour incoming from the evaporator is absorbed to make a weak LiBr-H2O solution (stream 26). This weak solution is then pumped.

(PUM 2) to a higher pressure to the desorber (stream 27) and is passed through the heat exchanger (HEX3) to gain some heat (stream 28) and return to the desorber. The cycle continues in this order. The heat released in the form of flue gases (stream 57) from the combustion of fuel obtained from biomass gasification flows to the hot water generating unit and transfers its heat energy to the hot water generator for domestic hot water supply. Exiting (stream 60) into a heat exchanger (HEX) and transferring energy to the incoming water (stream 61). The spent flue gases (stream 70) leave HEX through the stack, while heated water (stream 62) and hot water by-product (stream 64) from the proton exchange membrane (PEM) electrolyzer mix uniformly as stream 63. A portion of the electric power generated from the Kalina cycle (stream 79) is used by electrolysis reaction to decompose the heated water (stream 63) in the PEM electrolyzer, which yields hydrogen (stream 65) going into the H2 storage tank, oxygen and hot water mixture (stream 67) which goes through the O2 separator to split into oxygen (stream 78) going into the O₂ storage tank and hot water (stream 64) going as a portion of the input to feed the PEM electrolyzer. The chemical energy of the fuel, hydrogen (stream 68) and oxygen from the air, is converted into electricity (stream 81) in the fuel cell unit through a pair of redox reactions.

Thermodynamic Modelling and Analysis

This research work deployed thermodynamic modelling, which specifically dwelt on mass, energy, and exergy balances of each component of the subsystems of the multigeneration system through developed codes in the EES software [35].

Energy Modelling

The system is modelled using the energy flow equation at steady state conditions for a control volume. Thus, for the k^{th} component, the energy balance, since the potential and kinetic energy effects are negligible, is generally obtained as follows from Rajput [36]:

$$\dot{Q}_k + \sum_k \left| H_i + KE_i + PE_i \right| = \dot{W}_k + \sum_k \left| H_j + KE_j + PE_j \right| \quad (1)$$

The terms in Eq. (1) are represented as: \dot{Q}_k = heat rate to the kth component, \dot{W}_k = rate of work output from the k^{th} component, while H_i , KE_i , and PE_i , represent the enthalpy, kinetic energy, and potential energy, respectively, at the component inlet. Similar expressions are used for the control volume at the outlet.

However, since the potential and kinetic energy effects are negligible, Equation (1) is reduced to Equation (2) as:

$$\dot{Q}_k + \sum_k |H_i| = \dot{W}_k + \sum_k |H_j| \tag{2}$$

Equation (2) is applied to all components of the system; similarly, the mass balance is obtained at the component level with the term [36]:

$$\sum \dot{m}_i = \sum \dot{m}_j \tag{3}$$

Table 1. Summary of energy balances for the system

Component	Energy balance	
PTC	$\dot{m}_{54} h_{54} + E_{sun} = \dot{m}_{52} h_{52}$	
ORC vapour generator	$\dot{m}_{40}h_{40} + \dot{m}_{53}h_{53} = \dot{m}_{41}h_{41} + \dot{m}_{54}h_{54}$	
ORC turbine	$\vec{m}_{41} h_{41} = \vec{m}_{42} h_{42} + W_{ORC_{TURB}} + W_{ORC_{PUMP}} + W_{COMP}$	
ORC condenser 4	$\dot{m}_{50} h_{50} + \dot{m}_{42} h_{42} = \dot{m}_{51} h_{51} + \dot{m}_{43} h_{43}$	
ORC pump	$W_{ORC_{pump}} + m_{39} h_{39} = m_{40} h_{40}$	
ORC valve 6	$\dot{m}_{43} \dot{h}_{43} = \dot{m}_{44} \dot{h}_{44}$	
ORC evaporator 3	$\dot{m}_{44} h_{44} + \dot{m}_{45} h_{45} = \dot{m}_{38} h_{38} + \dot{m}_{46} h_{46}$	
ORC compressor	$\dot{m_{38}} h_{38} + W_{comp} = \dot{m_{77}} h_{77}$	
Kalina vapour generator	$\vec{m}_{52} h_{52} + \vec{m}_{23} h_{23} = \vec{m}_1 h_1 + \vec{m}_{53} h_{53}$	
Kalina separator 1	$\vec{m_1} h_1 = \vec{m_2} h_2 + \vec{m_3} h_3$	
Kalina separator 2	$\dot{m_5} h_5 = \dot{m_6} h_6 + \dot{m_8} h_8$	
Kalina turbine	$\dot{m_3} h_3 = \dot{m_5} h_5 + W_{Kal_{TURB}} + W_{PEM}$	
Kalina valve 3	$\dot{m_2}\dot{h}_2 = \dot{m_4}\dot{h}_4$	
Kalina valve 2	$\dot{m_6} \dot{h_6} = \dot{m_7} \dot{h_7}$	
Kalina valve 1	$\dot{m_9} \dot{h_9} = \dot{m_{10}} \dot{h_{10}}$	
Kalina condenser 1	$\dot{m_8} \dot{h_8} + \dot{m_{11}} \dot{h_{11}} = \dot{m_9} \dot{h_9} + \dot{m_{12}} h_{12}$	
Kalina evaporator 1	$\dot{m_{10}}\dot{h_{10}}+\dot{m_{13}}\dot{h_{13}}=\dot{m_{14}}\dot{h_{14}}+\dot{m_{17}}h_{17}$	
Kalina condenser 2	$\dot{m}_{19} \dot{h}_{19} + \dot{m}_{24} \dot{h}_{24} = \dot{m}_{20} \dot{h}_{20} + \dot{m}_{25} \dot{h}_{25}$	
Kalina HEX 1	$\dot{m_{18}}\dot{h_{18}}+\dot{m_{21}}\dot{h_{21}}=\dot{m_{19}}\dot{h_{19}}+\dot{m_{22}}h_{22}$	
Kalina HEX 2	$\dot{m}_{15} \dot{h}_{15} + \dot{m}_{22} \dot{h}_{22} = \dot{m}_{16} \dot{h}_{16} + \dot{m}_{23} h_{23}$	
Kalina pump 1	$W_{Kal_{pump}} + \dot{m_{20}} h_{20} = \dot{m_{21}} h_{21}$	
VAS desorber	$\vec{m}_{76} \vec{h}_{76} + \vec{m}_{28} \vec{h}_{28} = \vec{m}_{15} \vec{h}_{15} + \vec{m}_{29} h_{29} + \vec{m}_{34} \vec{h}_{34}$	
VAS condenser 5	$\dot{m}_{34} \dot{h}_{34} + \dot{m}_{73} \dot{h}_{73} = \dot{m}_{71} \dot{h}_{71} + \dot{m}_{74} \dot{h}_{74}$	
VAS valve 5	$\dot{m_{71}} \dot{h_{71}} = \dot{m_{72}} \dot{h_{72}}$	
VAS valve 4	$\dot{m_{30}} \dot{h_{30}} = \dot{m_{31}} \dot{h_{31}}$	
VAS evaporator 2	$\dot{m}_{36} \dot{h}_{36} + \dot{m}_{72} \dot{h}_{72} = \dot{m}_{37} \dot{h}_{37} + \dot{m}_{35} h_{35}$	
VAS HEX 3	$\dot{m}_{27} \dot{h}_{27} + \dot{m}_{29} \dot{h}_{29} = \dot{m}_{28} \dot{h}_{28} + \dot{m}_{30} h_{30}$	
VAS pump 2	$W_{VAS_{pump}} + \dot{m}_{26} h_{26} = \dot{m}_{27} h_{27}$	
VAS absorber	$\vec{m}_{31} \dot{\vec{h}}_{31} + \vec{m}_{35} \dot{\vec{h}}_{35} + \vec{m}_{32} \dot{\vec{h}}_{32} = \vec{m}_{33} \dot{\vec{h}}_{33} + \vec{m}_{26} h_{26}$	
Biomass combustor	$\dot{m}_{55} \dot{h}_{55} + \dot{m}_{56} \dot{h}_{56} = \dot{m}_{57} \dot{h}_{57}$	
Water heater	$\dot{m}_{57} \dot{h}_{57} + \dot{m}_{58} \dot{h}_{58} = \dot{m}_{59} \dot{h}_{59} + \dot{m}_{60} h_{60}$	
PEM HEX	$\dot{m}_{60} \dot{h}_{60} + \dot{m}_{61} \dot{h}_{61} = \dot{m}_{62} \dot{h}_{62} + \dot{m}_{70} h_{70}$	
PEM Electrolyser	$\dot{m}_{63} \dot{h}_{63} + W_{PEM} = \dot{m}_{67} \dot{h}_{67}$	
Oxygen separator	$m_{67} h_{67} = m_{64} h_{64} + m78 h_{78}$	

Parabolic Trough Collector Subsystem

The Parabolic Trough collectors (PTCs) receive energy from the sun as one of the energy sources of the multigeneration energy system. PTCs are eligible to deliver high temperatures up to 400 °C for heat production or electricity generation and are available in the market with several types. The energy balance in the PTC, for Equation (1), is obtained as:

$$\dot{m}_{54}h_{54} + E_{sun} = \dot{m}_{52}h_{52} \tag{4}$$

The Actual useful heat gain from a concentrating type collector is defined with the Hottel–Whilier equation from Kalogirou [37] and Tyagi et al. [38]:

$$E_{sun} = F_r A_a \left[C(\rho \alpha) S_t - U_L (T_{col} - T) - \varepsilon \sigma (T_{col}^4 - T_o^4) \right]$$
 (5)

where, F_r is the collector heat removal factor, A_a is the aperture area, C is the concentration ratio, ρ , α , ε , and σ are reflectivity, absorptivity, and emissivity and Stephan Boltzman constant, U_L is the overall heat loss coefficient and can be directly obtained or determined using equations in Tyagi et al. [38], S_t is global solar radiation, and T is the collector temperature. The heat removal factor of the collectors can be defined as follows:

$$F_r = \frac{mc_p}{A_r U_L} \left[1 - e^{\frac{-A_r U_L F}{mc_p}} \right] \tag{6}$$

Here, the unknowns F, \dot{m} , c_p , and A_r are collector efficiency, working fluid mass flow rate, specific heat and reflector area, respectively. The connection between the aperture and reflector area can be written in terms of concentration ratio as follows [38]

$$C = \frac{A_r}{A_a} \tag{7}$$

The definition for aperture area is [38]:

$$A_a = (\omega - D_c)L \tag{8}$$

where *L* is the collector length, ω is the collector width and D_c is the collector cover diameter.

From Equation (1), the related energy equations for each of the components and subsystems are formulated for the multigeneration system in Table 1. The properties of the different hardwood species [39] used as biomass are presented in Table 2

Exergy Modelling

The exergy modelling of the integrated energy system is performed at steady state conditions using the second law of thermodynamics. Exergy-based modelling has the potential to identify components in the system with large irreversibilities and quantify them. The analysis considers each component as a control volume while applying the general exergy balance expression in Equation. (39) from Bejan and Tsatsaronis [40] as:

 Table 2. Elemental composition and combustion properties of some the hardwood species [30]

Wood Species	Common Name (English)	C (%)	H (%)	(%) O	(%) N	S (%)	GCV (MJ/kg)	Density (g/cm³)	MC (%)	Ash (%)	FVI
Acacia sp	Acacia	49.05	5.46	45.13	0.32	0.03	18.944	1.125	89.6	5.38	4092.19
Afzelia africana	African mahogany / Apa	48.26	5.27	46.15	0.29	0.03	18.356	0.792	10.00	6.28	2315.00
Celtis sp	Hackberry	45.06	5.04	49.62	0.25	0.03	16.652	0.658	9.84	4.73	2354.11
Brachystegia eurycoma	African walnut (locally)	47.72	5.74	46.35	0.18	0.02	18.673	0.735	9.52	5.35	2694.64
Bombax bounopozense	Red silk cotton tree	45.38	5.53	48.94	0.14	0.01	17.372	1.007	10.17	5.78	2976.02
Blighia sapida	Akee apple	46.66	5.16	47.88	0.28	0.03	17.511	0.582	9.84	7.24	1430.51
Piptadeniastrum africanum	Dahoma	42.67	5.60	51.48	0.24	0.02	16.272	0.843	10.17	4.87	2769.59
Cleistopholis partens	Salt tree	49.11	5.33	45.34	0.20	0.02	18.792	0.751	10.53	5.85	2290.98
Triplochiton scleroxylon	Obeche / African whitewood	46.28	5.46	48.07	0.17	0.02	17.692	1.032	60.6	82.9	2962.52
Albizia sp	West African albizia	41.07	5.53	53.16	0.22	0.02	15.475	1.056	8.62	7.33	2586.38

Table 3. Summary of component exergy balances for the system

Component	Component exergy balance	Exergy of fuel	Exergy of product
PTC	$\dot{E}_{54} + \dot{E}_{\dot{Q}_{sun}} = \dot{E}_{52} + \dot{E}D$	ĖQsun	\dot{E}_{52} - \dot{E}_{54}
ORC vapour gen.	$\dot{E}_{40} + \dot{E}_{53} = \dot{E}_{41} + \dot{E}_{54} + \dot{E}D$	\dot{E}_{54} - \dot{E}_{53}	\dot{E}_{40} - \dot{E}_{41}
ORC turbine	$\dot{E}_{41} = \dot{E}_{42} + \dot{E}_{WORC_{TURB}} + \dot{E}_{WORC_{PUMP}} + \dot{E}_{WCOMP} + \dot{E}D$	\dot{E}_{41} - \dot{E}_{42}	$\dot{E}_{W_{ORC_{TURB}}} + \dot{E}_{W_{ORC_{PUMP}}} + \dot{E}_{W_{COMP}}$
ORC cond. 4	$\dot{E}_{50} + \dot{E}_{42} = \dot{E}_{51} + \dot{E}_{43} + \dot{E}D$	\dot{E}_{42} - \dot{E}_{43}	Ė51 - Ė ₅₀
ORC pump	$\dot{E}_{39} + \dot{E}_{WORC_{pump}} = \dot{E}_{40} + \dot{E}D$	\dot{E}_{WORC} pump	\dot{E}_{40} - \dot{E}_{39}
ORC valve 6	$\dot{E}_{43} = \dot{E}_{44} + \dot{E}D$	\dot{E}_{43}	\dot{E}_{44}
ORC evap. 3	$\dot{E}_{44} + \dot{E}_{45} = \dot{E}_{38} + \dot{E}_{46} + \dot{E}D$	\dot{E}_{45} - \dot{E}_{46}	\dot{E}_{38} - \dot{E}_{44}
ORC comp.	$\dot{E}_{38} + \dot{E}_{W_{comp}} = \dot{E}_{77} + \dot{E}D$	$\dot{E}_{W_{comp}}$	\dot{E}_{77} - \dot{E}_{38}
Kalina vap. gen.	$\dot{E}_{52} + \dot{E}_{23} = \dot{E}_1 + \dot{E}_{53} + \dot{E}D$	\dot{E}_{52} - \dot{E}_{53}	\dot{E}_1 - \dot{E}_{23}
Kalina sep. 1	$\dot{E}_1 = \dot{E}_2 + \dot{E}_3 + \dot{E}D$	\dot{E}_1	$\dot{E}_2 + \dot{E}_3$
Kalina sep. 2	$\dot{E}_5 = \dot{E}_6 + \dot{E}_8 + \dot{E}D$	\dot{E}_5	$\dot{E}_6 + \dot{E}_8 + \dot{E}D$
Kalina turb.	$\dot{E}_3 = \dot{E}_5 + \dot{E}_{W_{Kal_{TURB}}} + \dot{E}_{W_{PEM}} + \dot{E}D$	\dot{E}_3 - \dot{E}_5	$\dot{E}_{W_{Kal_{TURB}}} + \dot{E}_{W_{PEM}}$
Kalina valve 3	$\dot{E}_2 = \dot{E}_4 + \dot{E}D$	\dot{E}_2	\dot{E}_4
Kalina valve 2	$\dot{E}_6 = \dot{E}_7 + \dot{E}D$	\dot{E}_6	\dot{E}_7
Kalina valve 1	$\dot{E}_9 = \dot{E}_{10} + \dot{E}D$	\dot{E}_{9}	\dot{E}_{10}
Kalina cond. 1	$\dot{E}_8 + \dot{E}_{11} = \dot{E}_9 + \dot{E}_{12} + \dot{E}D$	\dot{E}_8 - \dot{E}_9	\dot{E}_{12} - \dot{E}_{11}
Kalina eva. 1	$\dot{E}_{10} + \dot{E}_{13} = \dot{E}_{14} + \dot{E}_{17} + \dot{E}D$	\dot{E}_{13} - \dot{E}_{14}	\dot{E}_{17} - \dot{E}_{10}
Kalina condenser 2	$\dot{E}_{19} + \dot{E}_{24} = \dot{E}_{20} + \dot{E}_{25} + \dot{E}D$	\dot{E}_{19} - \dot{E}_{20}	\dot{E}_{25} - \dot{E}_{24}
Kalina HEX 1	S	\dot{E}_{18} - \dot{E}_{19}	\dot{E}_{22} - \dot{E}_{21}
Kalina HEX 2	$\dot{E}_{15} + \dot{E}_{22} = \dot{E}_{16} + \dot{E}_{23} + \dot{E}D$	\dot{E}_{15} - \dot{E}_{16}	\dot{E}_{23} - \dot{E}_{22}
Kalina pump 1	$\dot{E}_{W_{Kal_{pump}}} + \dot{E}_{20} = \dot{E}_{21} + \dot{E}D$	$\dot{E}_{W_{Kal_{pump}}}$	\dot{E}_{21} - \dot{E}_{20}
VAS desorber	$\dot{E}_{76} + \dot{E}_{28} = \dot{E}_{15} + \dot{E}_{29} + \dot{E}_{34} + \dot{E}D$	$\dot{E}_{76} + \dot{E}_{28}$	$\dot{E}_{15} + \dot{E}_{29} + \dot{E}_{34}$
VAS cond. 5	$\dot{E}_{34} + \dot{E}_{73} = \dot{E}_{71} + \dot{E}_{74} + \dot{E}D$	\dot{E}_{34} - \dot{E}_{71}	\dot{E}_{74} - \dot{E}_{73}
VAS valve 5	$\dot{E}_{71} = \dot{E}_{72} + \dot{E}D$	\dot{E}_{71}	\dot{E}_{72}
VAS valve 4	$\dot{E}_{30} = \dot{E}_{31} + \dot{E}D$	\dot{E}_{30}	\dot{E}_{31}
VAS evap. 2	$\dot{E}_{36} + \dot{E}_{72} = \dot{E}_{37} + \dot{E}_{35} + \dot{E}D$	\dot{E}_{36} - \dot{E}_{37}	\dot{E}_{35} - \dot{E}_{72}
VAS HEX 3	$\dot{E}_{27} + \dot{E}_{29} = \dot{E}_{28} + \dot{E}_{30} + \dot{E}D$	\dot{E}_{29} - \dot{E}_{30}	\dot{E}_{28} - \dot{E}_{27}
VAS pump 2	$\dot{E}_{WVAS_{pump}} + \dot{E}_{26} = \dot{E}_{27} + \dot{E}D$	$\dot{E}_{W_{V\!AS_{pump}}}$	\dot{E}_{27} - \dot{E}_{26}
VAS absorber	$\dot{E}_{31} + \dot{E}_{35} + \dot{E}_{32} = \dot{E}_{33} + \dot{E}_{26} + \dot{E}D$	$\dot{E}_{31} + \dot{E}_{35}$	$\dot{E}_{26} + \dot{E}_{33} - \dot{E}_{32}$
Biomass combustor	$\dot{E}_{55} + \dot{E}_{56} = \dot{E}_{57} + \dot{E}D$	$\dot{E}_{55} + \dot{E}_{56}$	\dot{E}_{57}
Water heater	$\dot{E}_{57} + \dot{E}_{58} = \dot{E}_{59} + \dot{E}_{60} + \dot{E}D$	\dot{E}_{57} - \dot{E}_{60}	\dot{E}_{59} - \dot{E}_{58}
PEM HEX	$\dot{E}_{60} + \dot{E}_{61} = \dot{E}_{62} + \dot{E}_{70} + \dot{E}D$	\dot{E}_{60} - \dot{E}_{62}	\dot{E}_{70} - \dot{E}_{61}
PEM Electrolyser	$\dot{E}_{63} + \dot{E}_{W_{PEM}} = \dot{E}_{67} + \dot{E}_{65} + \dot{E}D$	\dot{E}_{63}	$\dot{E}_{67} + \dot{E}_{65}$
Oxygen separator	$\dot{E}_{67} = \dot{E}_{64} + \dot{E}_{78} + \dot{E}D$	Ė ₆₇	$\dot{E}_{64} + \dot{E}_{78}$

$$\dot{E}_{Q_k} + \sum_k \dot{E}_i = \dot{E}_{W_k} + \sum_k \dot{E}_j + \dot{E}_{D_k}$$
 (9)

Where \dot{E}_{D_k} is the exergy destruction rate, \dot{E}_{Q_k} is the exergy flow rate associated with heat transfer, \dot{E}_{W_k} is the rate of work done within the control volume, $\sum_k \dot{E}_i$ and $\sum_k \dot{E}_j$ are the sums of the exergy flow rate in and out of the control volume, respectively. The subscript 'k' represents the kth component. The exergy associated with work and heat is defined as [40]:

$$\dot{E}_{W_k} = \dot{m}_i \big| h_i - h_i \big| \tag{10}$$

$$\dot{E}_{Q_k} = Q_k \left| 1 - \frac{T_0}{T_k} \right| \tag{11}$$

The exergy destruction can also be expressed in terms of product and fuel exergy as:

$$\dot{E}_{D,k} = \dot{E}_{F,k} - \dot{E}_{Pk} \tag{12}$$

The exergy efficiency, ψ_k , and the exergy destruction ratio, $Y_{D,k}$, are equally defined for the k^{th} component as [40]:

$$\psi_k = \frac{\dot{E}_{Pk}}{\dot{E}_{Fk}} \tag{13}$$

$$Y_{D,k} = \frac{E_{D,k}}{\dot{E}_{F,total}} \tag{14}$$

Parabolic trough collector subsystem

The exergy balance in the PTC, for Equation (9), is obtained as:

$$\dot{E}_{54} + \dot{E}_{\dot{Q}_{sun}} = \dot{E}_{52} + \dot{E}_{D} \tag{15}$$

The amount of solar heat ratio collected by the solar collectors and transferred to the working fluid can be defined as [37]:

$$\dot{Q}_{sun} = F_r A_a S_t \eta_r C_r \tag{16}$$

Here, C_r represents the number of collector rows and η_r represents receiver efficiency. Equation (16) is used to calculate heat exergy

input to the system since the collector and heat exchanger efficiencies are not included in Equation (5)

From Equation (9) the related exergy balance, the exergy of fuel, and the exergy of product around the state points in each component of the subsystems of the multigeneration system are expressed below in Table 3.

Thermophysical Properties of the Hybrid Nanofluid

The equations used to calculate the hybrid nanofluid characteristics are provided in this section and are adapted from the source, Takabi & Salehi [41].

In the equations below, "1" represents a Multi-walled carbon nanotube (MWCNT) nanoparticle, "2" represents Aluminium Oxide (Al_2O_3) nanoparticle, "bf" represents the base fluid Therminol VP1, and "hnf" represents the hybrid nanofluid.

The density of the hybrid nanofluid is derived below (Equation (17)) as an extended form of single-particle nanofluid, which showed great agreement with experimental results [41]:

$$\rho_{\rm hnf} = \varphi_1 \rho_1 + \varphi_2 \rho_2 + (1 - \varphi) \rho_{\rm bf} \tag{17}$$

 φ is the total volume concentration of two types of nanoparticles scattered in a hybrid nanofluid, computed as [41]:

$$\varphi = \varphi_1 + \varphi_2 \tag{18}$$

Equation (19) below is an extended form of the single-particle nanofluid used in specifying the heat capacity of the hybrid nanofluid [41]:

$$C_{\rm hnf} = \frac{\varphi_1 \rho_1 c_1 + \varphi_2 \rho_2 c_2 + (1 - \varphi) \rho_{bf} c_{bf}}{\rho_{\rm hnf}} \tag{19}$$

In addition, the thermal conductivity of hybrid nanofluid, which is defined according to the Maxwell Model, is derived below (Equation (20)) as an extended form of single-particle nanofluid, which showed great agreement with experimental results [41]:

$$\frac{k_{\text{hnf}}}{k_{\text{bf}}} = \left(\frac{(\varphi_1 k_1 + \varphi_2 k_2)}{\varphi} + 2k_{\text{bf}} + 2(\varphi_1 k_1 + \varphi_2 k_2) - 2\varphi k_{\text{bf}}\right) \times \left(\frac{(\varphi_1 k_1 + \varphi_2 k_2)}{\varphi} + 2k_{\text{bf}} - (\varphi_1 k_1 + \varphi_2 k_2) + \varphi k_{\text{bf}}\right)^{-1}$$
(20)

Plant Performance Indices

Several plant performance indices were considered in the plant, including the Kalina turbine and pump work,

Table 4. Summary of key system performance indices

Performance index	Expression
Kalina turbine work	$m_3 h_3 - h_5 $
Kalina power requirement	$m_{20} \left h_{21} - h_{20} \right $
Kalina evaporator of cooling	$m_{17} \left h_{17} - h_{10} \right $
Kalina exergy of cooling	$ ex_{10} - ex_{17} $
ORC turbine output	$m_{41} \left h_{41} - h_{42} \right $
ORC pump work	$m_{39} \left h_{40} - h_{39} \right $
ORC compressor work	$m_{77} \left h_{77} - h_{38} \right $
ORC evaporator cooling	$m_{38} \left h_{38} - h_{44} \right $
ORC evaporator exergy of cooling	$ ex_{44} - ex_{38} $
PTC heat rate	$m_{52} \left h_{52} - h_{54} \right $
PTC exergy of heat	$ ex_{52} - ex_{54} $
VAS cooling rate	$m_{72} \left h_{72} - h_{35} \right $
VAS exergy of cooling	$ ex_{72} - ex_{35} $

Table 5. Model validation of present work with (Parikhani et al. [42] for Kalina cycle subsystem

Parameter	Reference [42]	Present work
System working fluid	Ammonia-water	Ammonia-water
Mass flow rate (Kg/s)	2.917	2.917
Ammonia concentration at turbine outlet (%)	99.97	83.06
Turbine inlet Temperature (°C)	160.2	160.2
Turbine inlet pressure (bars)	30	30
Turbine outlet pressure (bars)	2.986	2.986
Net power output (kW)	886.3	941.3

exergy of refrigeration, both for the Kalina and ORC, as well as ORC turbine work. All performance indices and the corresponding developed relationships are shown in Table 4, following the nomenclature in Figure 1.

RESULTS VALIDATION

To validate the thermodynamic simulation results for the proposed Multigeneration system, a suitable code is written in Engineering Equation Solver (EES) software to compare the obtained findings to those in the literature. In this study, four case studies from the literature are chosen, and each is simulated in a constant situation. These case studies include the KC, ORC, VAS subsystem, and PEM electrolyzer system. Validation for each case study is performed below.

Validation of Kalina Cycle Subsystem

In the first case study, a KC is selected from Parikhani et al. [42], and simulated under constant input parameters. In this simulation, some of the KC design input parameters of [42] were plugged into the KC of the present work model. It can be expressed that the results of the current investigation properly corroborate the results of [42], with some improvements in performance indices. According to Table 5, a performance parameter (i.e. net output power) is selected, and the calculated value is compared with the literature. There is a good agreement between the obtained result in the present model and those reported in the literature.

Validation Of Organic Rankine Cycle Subsystem

For the second case study, the results of the model for the Organic Rankine Cycle system are presented in Table 6. Some of the ORC design input parameters of [43] were plugged into the ORC of the present work model. It can be stated that the results of the current investigation properly verify the results of Ozturk & Dincer [43], with some enhancements in the performance indices. From Table 6, two performance parameters (i.e., Turbine Power Output and Pump work) are selected, and the calculated values are compared with the literature. This comparison of the different parameters validates well with the literature.

Validation of Vapour Absorption Subsystem

Presented in Table 7 is the third case study, which is the vapor absorption system (VAS). In the simulation, some of the VAS design input parameters of Karaca and Dincer [44], were substituted into the VAS of the present work model. From Table 7, two performance parameters (i.e. evaporator cooling rate and energetic COP) are selected and the calculated values are compared with the literature. This comparison of the different parameters, agrees well with the literature.

Validation of PEM Electrolyzer Subsystem

The final but not least significant verification step is using a PEM electrolyzer. In the mathematical modelling of the PEM electrolyzer, the operating temperature is set at 90°C, the power supplied is 4.07kW, and the oxygen and hydrogen pressures are fixed at 1 bar. Based on Table 8, a performance indicator (i.e., hydrogen production rate) is

Table 6. Model validation of the present work with Ozturk & Dincer, [43] for the ORC generation subsystem

Parameter	Reference [43]	Present work
System working fluid	Isobutane	Isobutane
Mass flow rate (Kg/s)	34.24	34.24
Turbine inlet Temperature (°C)	146.8	146.8
Turbine inlet pressure (bars)	32.5	32.5
Turbine outlet pressure (bars)	4.10	4.10
Turbine Power Output (kW)	2436	3110
Pump work (kW)	234	182.2

Table 7. Model validation of present work with Karaca & Dincer [44] for the VAS subsystem

Parameter	Reference [44]	Present work
System working fluid	Ammonia-water	Ammonia-water
Mass flow rate (Kg/s)	0.0089	0.0089
Pressure across the evaporator (bars)	4.62	4.62
VAS cooling rate (kW)	5.08	4.546
Energetic COP	0.96	0.8783

Table 8. Model validation of the p	present work with Khanmohammadi et al. [45] for PEM electroly	zer
---	---	-----

Parameter	Reference [45]	Present work
Electrolyzer hot water Mass flow rate (Kg/s)	-	1.99
Electrolyzer temperature (°C)	95	95
Electrolyzer Pressure (bar)	1	1
Electricity feed to electrolyzer (kW)	4.07	4.07
Hydrogen production rate (kg/hr)	0.245	0.255

selected, and the calculated value is compared with the literature. It can be expressed that the results of the current investigation substantiate the results of Khanmohammadi et al. [45] as seen in Table 8, with some improvements in performance indices. A minor discrepancy is attributed to the different design operating conditions, like the unavailable or varying mass flow rate of water. Since the mass flow rate of water affects hydrogen production if it is insufficient, but once sufficient, the hydrogen flow rate increases with an increase in power supplied, as long as efficiency losses at high power are managed.

RESULTS AND DISCUSSION

This paper investigates the thermodynamic performance of a solar power-biomass-assisted multigeneration system for the production of electricity, cooling, heating, hydrogen, and hot water from the energetic and exergetic analysis perspectives. The design data and thermodynamic

computation of this modelled investigation at the component level were simulated utilizing a generated source code in EES. Table 9 shows the design data used for the analysis. In conducting the energy and exergy assessments of the solar-biomass integrated multigeneration system, values of mass flow rate, temperature, pressure, specific enthalpy, specific entropy and exergy are serially determined for each state of the system as tabulated in Table 10. These were considered and evaluated using the design conditions in Table 9.

As obtained in Table 4, the major performance indices of the plant are shown in Table 11, and comprises the power output and cooling from both the ORC and KC subsystems. The system has a total power output of 964 kW, with 276.03 kW from the ORC and 145.28 kW from the Kalina system. Also, cooling from the Kalina system after turbine expansion and separation resulted in 129.6 kW of cooling with an evaporator temperature of -33.5 °C. Since the analysis involved the second law analysis, the exergy of cooling in

Table 9. System initial design data

Parameter	Schematic label	Unit	Value
PTC heat rate	QPTC	kW	1295
ORC TIT	t_{41}	°C	130
ORC TIP	P_{41}	Bar	25
ORC intermediate pressure	P_{44}	Bar	0.671
ORC condenser pressure	P_{42}	Bar	4.79
ORC refrigerant mass flow rate	$\dot{m_{41}}$	kg/s	2
Kalina TIT	t_3	°C	150
Kalina TIP	P_3	Bar	20
Ammonium water concentration	x_{21}	%	28
Kalina evaporator pressure	t_{10}	Bar	-34
Kalina condenser pressure	P_8	Bar	6.993
Ammonium water mass flow rate	$\dot{m_{21}}$	kg/s	1.3
VAS generator pressure	P_{34}	Bar	0.07904
VAS generator temperature	t_{34}	°C	80
VAS absorber pressure	P_{35}	Bar	0.008635
PEM electrolyzer temperature	t_{63}	°C	95
Biomass flow rate	m_{56}	kg/s	0.75

Table 10. The systems' operating thermodynamic properties

S/No	$\dot{m}\left(\frac{kg}{s}\right)$	t (°C)	P (bar)	$h\left(\frac{kJ}{kg}\right)$	$s\left(\frac{kJ}{kg.K}\right)$	E(kW)
1	1.3	150	20	583.3	2.094	161.5
	1.215	150	20	498.9	1.87	115
	0.08468	150	20	1796	5.315	41.55
	1.215	61.9	0.8	498.9	2.053	48.45
	0.08468	108.8	6.993	1610	5.315	25.87
i	0.005263	108.8	6.993	322.2	1.411	0.2296
	0.005263	56.7	0.8	322.2	1.476	0.1273
	0.07942	108.8	6.993	1697	5.578	25.59
	0.07942	18.8	6.993	-28.4	0.2503	14.63
0	0.07942	-33.5	0.8	-28.4	0.349	12.3
1	1.311	25	1.013	104.3	0.3651	0
2	1.311	50	1.013	208.8	0.7018	5.446
3	5.379	25	1.013	298.4	5.695	0
4	5.379	1	1.013	274.3	5.611	5.518
5	1.221	51.9	0.8	293	1.431	23.61
6	1.221	41.9	0.8	116.5	0.8817	8.093
7	0.07942	53.9	0.8	1604	6.341	0.1462
8	1.3	42.9	0.8	207.4	1.216	12.9
9	1.3	32.9	0.8	34.48	0.6622	2.714
0	1.3	25	0.8	-73.38	0.3073	-0.03079
1	1.3	25.1	20	-71.24	0.3073	2.743
2	1.3	40.1	20	-6.966	0.5177	4.796
3	1.3	55.1	20	57.31	0.7183	10.67
4	1.342	25	1.013	104.3	0.3651	0
5	1.342	50	1.013	208.8	0.7018	5.572
6	7.237	35	0.008635	85.05	0.2104	2.085
7	7.237	35	0.07905	85.08	0.2104	2.313
8	7.237	64	0.07905	144.1	0.394	33.81
9	7.037	80	0.07905	181.8	0.4761	63.6
0	7.037	45	0.07905	111.3	0.2657	8.349
1	7.037	35	0.008635	91.56	0.2025	2.062
2	12.7	25	1.013	104.3	0.3651	0
3	12.7	35	1.013	146.1	0.5031	8.711
4	0.2	80	0.07905	2649	8.452	27.02
5	0.2	5	0.008635	2510	9.029	-35.25
6	2.289	25	1.013	298.4	5.695	0
7	2.289	33	1.013	306.5	5.722	0.2185
8	2	5.5	0.671	408.4	1.748	-13.52
)	2	25	1.478	232.3	1.113	13.16
O	2	25.8	25	234	1.113	16.67
1	2	130	25	389.7	1.556	63.73
2	2	61.4	4.79	377.9	1.556	40.2
3	2	61.4	4.79	282.1	1.27	19.34
4	2	5.5	0.671	282.1	1.295	4.205
5	11.97	25	1.013	298.4	5.695	0
6	11.97	4	1.013	277.3	5.622	9.338

Table 10. The systems' operating thermodynamic properties (continued)

S/No	$\dot{m} \left(\frac{kg}{s} \right)$	t (°C)	P (bar)	$h\left(\frac{kJ}{kg}\right)$	$s\left(\frac{kJ}{kg.K}\right)$	E(kW)
47	-	-	-	-	-	-
48	3.647	25	1.013	104.3	0.3651	0
49	3.647	50	1.013	208.8	0.7018	15.14
50	1.835	25	1.013	104.3	0.3651	0
51	1.835	50	1.013	208.8	0.7018	7.618
52	3.854	180	1.813	903	-	731.6
53	3.854	101	19.6	664.1	-	306.8
54	3.854	65	19.4	567.1	-	153.4
55	4.433	25	1.013	298.4	5.695	0
56	0.75	25	1.013	-8442	1.362	16273
57	5.183	450	1.013	738.4	6.607	871.6
58	2.034	25	1.013	104.3	0.3651	0
59	2.034	90	1.013	376.4	1.191	52.87
60	5.183	350	1.013	631.6	6.448	563.5
61	1.847	25	1.013	104.3	0.3651	0
62	1.847	95	1.013	397.5	1.249	55.18
63	1.847	95	1.013	397.5	1.249	55.18
64	1.846	95	1.013	397.5	1.249	55.16
65	0.00006612	95	1.013	4937	56.4	0.006792
66	-	-	-	-	-	-
67	1.847	95	1.013	397.5	1.249	0.00346
68	-	-	-	-	-	-
69	-	-	-	-	-	-
70	5.183	250	1.013	527.1	6.266	304.1
71	0.2	55	0.07905	2602	8.313	25.84
72	0.2	54.1	0.008635	2602	9.334	-35.01
73	0.06503	25	1.013	104.3	0.3651	0
74	0.06503	60	1.013	250.6	0.8294	0.5187
75	-	-	-	-	-	-
76	1.221	61.9	0.8	498.1	2.051	48.57
77	2	25.2	1.478	422.8	1.752	13.25

Kalina evaporator was recorded as 12.15 kW. In the VAS, at an evaporator temperature of 5 °C, 18.4 kW of refrigeration was achieved, with a corresponding 0.24 kW of exergy of cooling. The PTC contributes about 311.4 kW and 683.8 kW of heat to power the vapour generators of the ORC and KC systems, respectively. The total net output of the system was simulated as 964.9 kW, with 93.32 kW of exergy, while the system's net heat input from the biomass combustor was 3827 kW. The energy and exergy efficiencies of the plant was recorded as 52.2 % and 16.14 %, respectively.

Parametric Study

The surrounding temperature influences most thermodynamic systems in their operation. For example, changes

in the surrounding temperature might occasionally lead to an increase or decrease in system performance. The impact of variations in ambient temperature on the total energy and exergy inputs into the integrated energy system is shown in Figure 2. The results indicate that the total energy input is 1848 kW. This remained relatively constant when ambient temperature varied from 290 to 310 $^{\rm o}{\rm K}$ for the reason that energy input is not affected by varying environment temperature conditions. Whereas for exergy input, at the same ambient temperature range from 290 to 310 $^{\rm o}{\rm K}$, it decreases linearly from 587.8 to 564.1 kW as exergy loss increases.

Figure 3 illustrates the impact of ORC turbine inlet temperature on the ORC turbine output. Between 120 to 150 °C, the turbine output power increased steadily from 17.74

Table 11. Summary of performance indices of the energy system

Performance index	Unit	Value
Kalina turbine work	kW	15.68
Kalina pump power requirement	kW	2.775
Kalina evaporator of cooling	kW	129.6
Kalina exergy of cooling	kW	12.15
ORC turbine output	kW	23.53
ORC pump work	kW	3.515
ORC compressor work	kW	28.89
ORC evaporator cooling	kW	252.5
ORC evaporator exergy of cooling	kW	17.73
PTC heat rate	kW	1295
PTC exergy of heat	kW	578.1
VAS cooling rate	kW	18.4
VAS exergy of cooling	kW	0.2358
Total energy output	kW	964.9
Total exergy output	kW	93.32
Total energy input	kW	1848
Total exergy input	kW	578.1
Energy efficiency	%	52.2
Exergy efficiency	%	16.14

to 59.13 kW. The sharp rise is due to the rise in the values of input enthalpies and exergies. Although the turbine power output increases with turbine inlet temperatures, it can be inferred that an optimum TIT of 137.5 $^{\circ}$ C exists corresponding to a turbine inlet pressure of 25 bar.

Figure 4. shows the impact of Kalina turbine inlet temperature (TIT) on both total energy and exergy efficiencies of the energy system. It is observed that an increase in Kalina turbine inlet temperature from 150 to 170 °C, results in an increase in both overall energy and exergy efficiencies.

Whereas the energy efficiency increased steadily from 52.2 to 78.4%, the exergy efficiency increased steadily to a peak of 18.42% at 162.9 °C, beyond this temperature, any further increase results in a decrease in power output due to operational disturbances.

Figure 5 demonstrates the impact of ORC turbine outlet pressure on the system performance index. By increasing the backpressure of the turbine from 3 to 6 bar, the exergy and energy efficiencies decrease by about 1% and 4.5%, respectively. However, at a very low turbine back pressure, the fluid can attain a two-phase zone after expansion with a resultant effect on turbine blades.

The influence of ORC turbine back pressure on turbine output is demonstrated in Figure 6. High turbine back pressures result in minimal turbine expansion with truncated turbine work. It was found that when the ORC turbine backpressure was increased from 3 to 6 bar, the ORC turbine power output decreased from 33.83 to 18.92 kW. The results demonstrate the validity of the model linking the operating parameters in the ORC and its components.

The impact on the total exergy and energy efficiencies due to changes in the Kalina turbine outlet pressure is shown in Figure 7. In the design simulation, the Kalina turbine outlet pressure was set at 6.993 bar. However, for this analysis, the Kalina turbine back pressure was varied between 5 and 8 bar; and within this range, the total system energetic and exergetic efficiencies decreased by about 1 % and 2.5 %, respectively. The results are consistent with the behavior of the energy generation system with regards to the value of turbine back pressure against the turbine power output capacity.

The results of the effect of generator temperature on VAS evaporator cooling is shown in Figure 8. The cooling rate with regard to energy and exergy considerations increases at a constant generator pressure of 0.07904 bar. The higher vapour generator temperature increases the heat input to the generator; thus, the refrigerant can absorb heat energy. This results in a higher concentration of refrigerant vapour

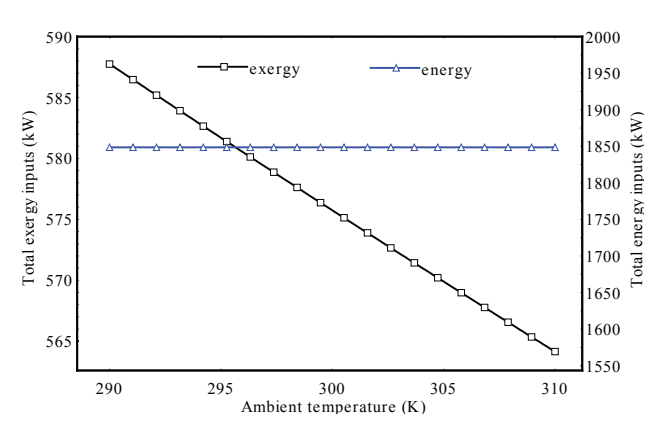


Figure 2. Ambient temperature effect on system total heat input.

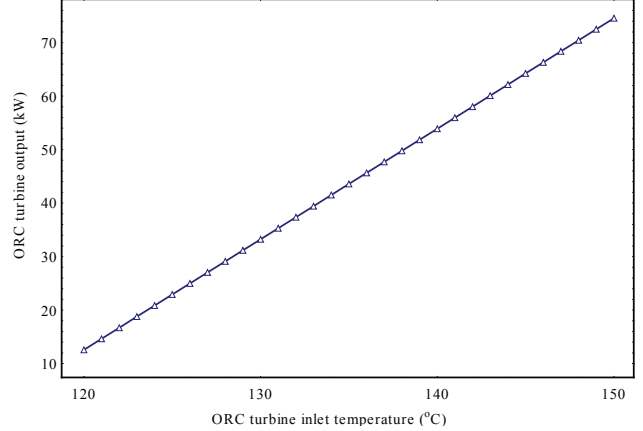


Figure 3. Effect of ORC TIT on ORC turbine output.

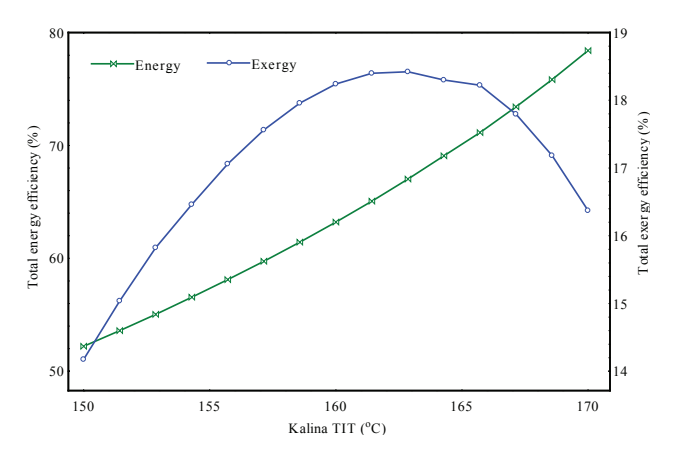


Figure 4. Effect of Kalina TIT on system's total efficiencies.

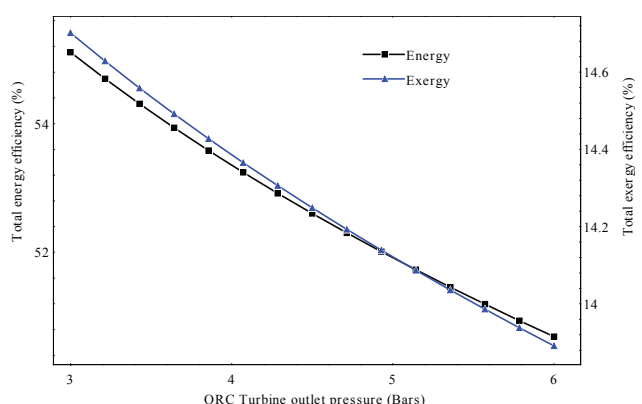


Figure 5. Effect of ORC turbine outlet pressure on total energy and exergy efficiencies.

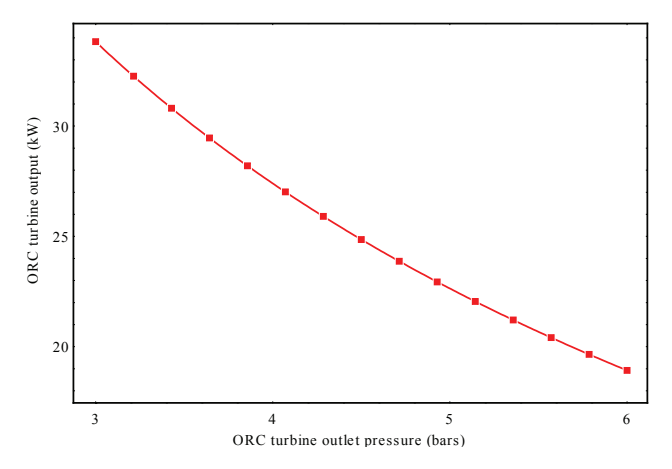


Figure 6. Effect of ORC turbine outlet pressure on ORC turbine power output.

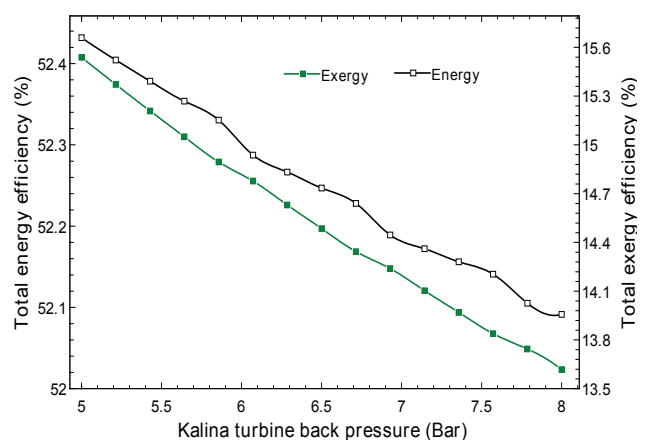


Figure 7. Effect of Kalina turbine back pressure on total energy and exergy efficiencies.

entering the condenser. Since the VAS relies on the absorption and desorption processes to create cooling, the higher concentration of refrigerant vapour in the condenser results in an increased cooling rate in the system. The magnitude of such an increase is depicted in Figure 8, where an additional 40 $^{\circ}$ C generator temperature increase resulted in an additional 20 kW of cooling in the evaporator with constant operating pressure.

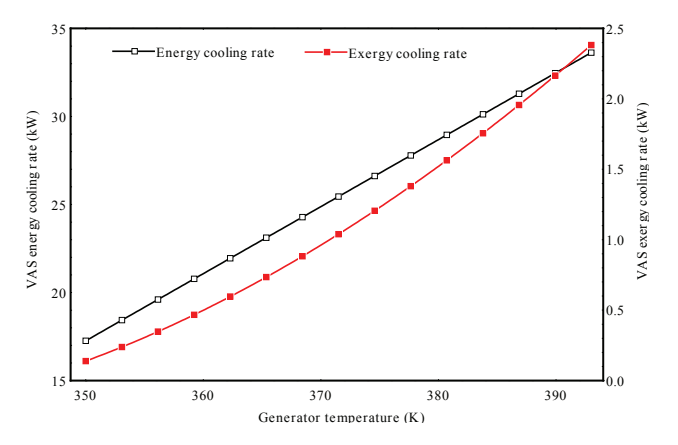
Vapour generator pressure on the cooling rate of the VAS evaporator was investigated with the result shown in Figure 9. Increasing the pressure in the vapour generator raises the boiling point of the refrigerant. This means that the refrigerant will need more energy to change from a liquid to a vapour state. As a result, the refrigerant is not able to absorb enough heat in the evaporator. The reduction of the cooling rate, both in energy and exergy, is thus experienced with higher vapour generator pressures.

The impact of the cell operating temperature of the PEM electrolyzer on the daily hydrogen production rate of the plant is seen in Figure 10. At increasing temperatures, the

PEM becomes more conductive, allowing for easier proton transport. This leads to a reduction in membrane resistance and improves the overall cell efficiency, thereby enhancing the hydrogen production rate. However, the results also show a decrease in the cell voltage when temperature was increased. The cell voltage dropped marginally to 1.15 volts for a cell temperature increase of 40 K. This drop can be attributed to the membrane connectivity due to increased proton migration triggering a voltage drop in the process.

Figure 11 demonstrates the energy balance around the domestic hot water heater, with hot water temperature fixed at 90 °C, gave an indication of the required biomass combustor outlet temperature and the quantity of hot water that can be produced. The quantity of hot water at 90 °C can be high with higher combustor outlet temperature as shown in Figure 11. The system can deliver up to 6000 liters of hot water at 90 °C for a combustor temperature of 425 °C.

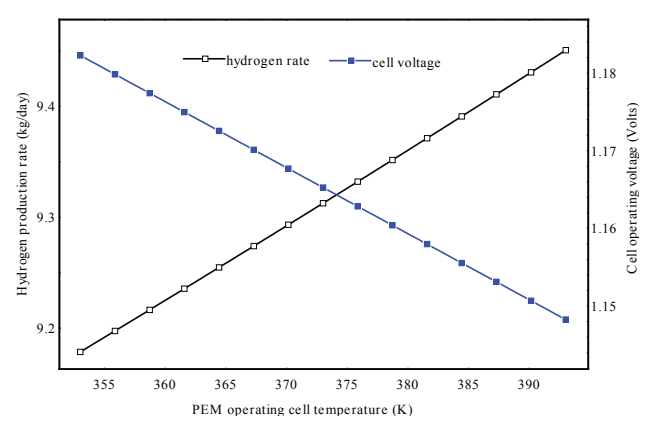
The result of hybrid nano fluid source temperature on the overall energy and exergy output of the system was investigated and shown in Figure 12. Without an additional



18.7 ——Energy cooling rate ——Exergy cooling

Figure 8. Effect of VAS generator temperature on evaporator cooling rate.

Figure 9. Effect of VAS generator pressure on evaporator cooling rate.



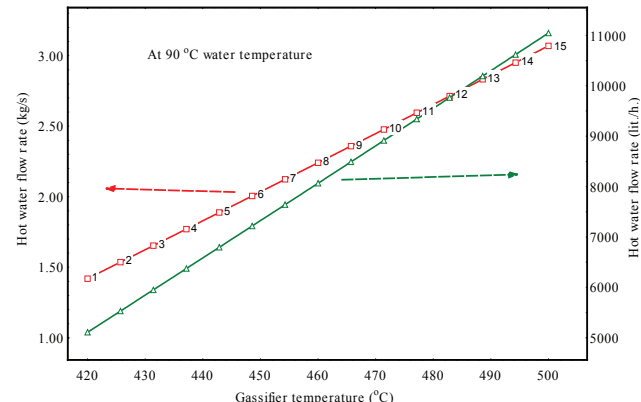
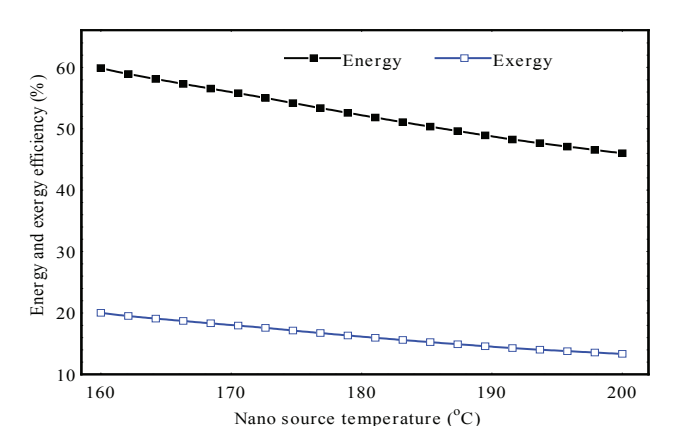


Figure 10. Effect of PEM temperature on cell voltage and hydrogen rate.

Figure 11. Effect of combustor temperature on domestic hot water production.

re-configuration of the system to reflect changes in turbine inlet parameters for the ORC and KC, an increase in the heat transfer of the hybrid nanofluid will result in additional heat transfer in the vapour generators of the two power

cycles. This is shown in Figure 12. Therefore, an increase in the nano operating temperature will overall result in lower energy and exergy efficiencies with large exergy destruction from the system.



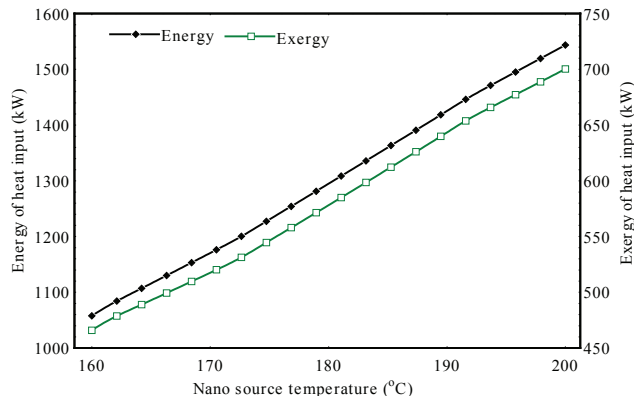


Figure 12. Nano source temperature effect on system total efficiencies.

Figure 13. Nano source temperature effect on system total heat inputs.

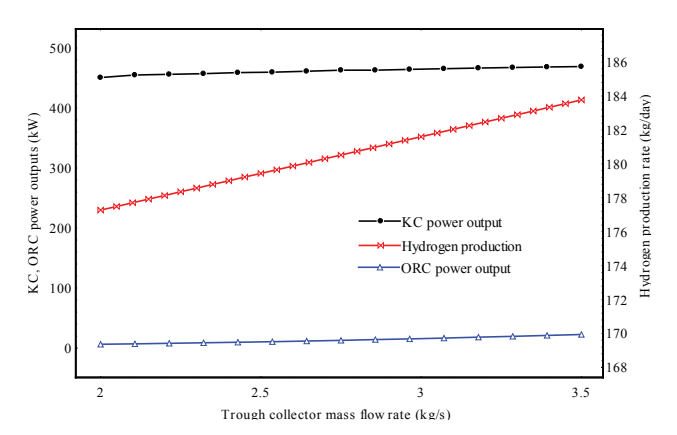


Figure 14. Variation of the collector mass flow rate with KC, ORC power outputs and hydrogen production rate.

The parametric effect of the hybrid Nano fluid source temperature was investigated on the overall energy and exergy inputs of the system in Figure 13. An increase in the Nano source temperature results in an increase in the overall energy input of the integrated energy system. Between the nano source temperatures of 155 °C to 180 °C, total energy input increased significantly from 1549 to 1848 kW. For the same source temperature range, the total exergy also increased from 435.8 to 578.1 kW. This increasing energy and exergy inputs with respect to higher source temperatures is so because both of these types of heat energy are functions of temperature since it is theoretically agreed upon that an increase in thermal energy yields an increase in temperature.

The effect of varying the trough collector mass flow rate on KC net power output, ORC net power output, and hydrogen production rate is demonstrated in Figure 14. As Parabolic Trough Collector (PTC) mass flow rate increases from 2 kg/s to 3.5 kg/s, the Kalina cycle net power output rises linearly by 4.1% from 450.8 kW to 469 kW, while the Organic Rankine Cycle (ORC) net power output increases non-linearly by 251% from 6.475 kW to 22.69 kW, accelerating beyond 2.75 kg/s. Concurrently, daily hydrogen production from the Proton Exchange Membrane (PEM) electrolyser grows steadily by 4.1% from 176.2 kg/day to 183.4 kg/day. These increases are attributed to enhanced heat transfer and improved thermal energy input, highlighting the benefits of optimizing PTC mass flow rate for improved performance in the multigeneration energy system.

CONCLUSION

This research paper examines the thermodynamic performance of a novel solar-biomass power based plant for hydrogen generation, from an energetic and exergetic viewpoints. This integrated energy system is designed for different purposes such as hot water, heating, electricity, cooling, and hydrogen productions. The parametric studies have been conducted with regard to a number of factors, including ambient temperature, the turbines inlet temperatures and the turbines output pressures. Here is a quick summary of the primary findings from the thermodynamic analysis:

- The ORC and Kalina subsystems are sustainable when run with R245fa and ammonium water as the respective working fluid.
- The system has a total power output of 964 kW, with 276.03 kW from the ORC and 145.28 kW from the Kalina system. Also, cooling from the Kalina system after turbine expansion and separation resulted in 129.6 kW of cooling with an evaporator temperature of -33.5 °C.
- The PTC contributes about 311.4 kW and 683.8 kW of heat to power the vapour generators of the ORC and Kalina systems, respectively. The total net output of the system was simulated as 964.9 kW, with 93.32 kW of exergy, while the system's net heat input from the biomass combustor was 3827 kW. The energy and exergy efficiencies of the plant was recorded as 52.2 % and 16.14 %, respectively.

Overall, the developed integrated energy systems model may easily replace conventional energy systems due to its higher energy and exergy efficiency and greater environmental performance. It could be an effective technique for incorporating solar energy into biomass gasification and reforming, allowing for the prediction and comparison of energetic and exergetic performance.

Further research will examine the dynamic behavior of the developed multigeneration plant, as the current work was carried out using a steady-state model, and it was observed that solar irradiance and biomass variations considerably affect efficiency. In order to determine appropriateness from a wider sustainability standpoint, the cost-effectiveness and eco-friendliness will also be assessed utilizing exergoeconomic and exergoenvironmental assessments.

NOMENCLATURE

Symbol

A_a	Aperture area (m²)
A_r	Reflector area (m²)
C	Concentration ratio
C_{hnf}	Heat capacity of the hybrid nanofluid (kJ/K)
c_p	Specific heat (J/kg·K)
$c_p \\ C_r$	Number of collector rows
D_c	Collector cover diameter (m)
\dot{E}_{W_k}	Exergy associated with work (kJ)
\dot{E}_{Qk}	Exergy associated with heat (kJ)
\dot{E}_{Dk}	Exergy destruction rate (kJ/s)
F	Collector efficiency (%)
F_r	Collector heat removal factor
H	Enthalpy (kJ)
h	Specific enthalpy (kJ/kg)

k	Thermal conductivity (kW/m.K)	O	Oxygen
L	Collector length (m)	ORC	Organic Rankine cycle
ṁ	Working fluid mass flow rate (kg/s)	PEM	Proton exchange membrane
P	Pressure	PTC	arabolic trough collector
\dot{Q}_k	Heat rate to the kth component (kJ/s)	PUM	Pump
S	Specific entropy (kJ/kg.K)	PV	Photovoltaics
S_t	Global solar radiation (kW/m²)	S	Separator & Sulphur
T	Collector temperature (K)	SAM	System Advisor Model software
t	Temperature (°C)	SGT	Solar-driven gas turbine
U_L	Overall heat loss coefficient (kW/m²K)	V	Valve
$egin{array}{c} U_L \ \dot{W_k} \end{array}$	Rate of work output from the kth component	VAS	Vapour absorption system
	(kJ/s)	VG	Vapour generator
Y_{Dk}	Exergy destruction ratio		

Greek symbols

- absorptivity α ε - emissivity - reflectivity ρ

- Density of the base fluid (kg/m³) ρ_{bf} - Density of the hybrid nanofluid (kg/m3) ρ_{hnf}

- Total volume concentratio

- Stephan Boltzman constant (kW/m²K⁴) σ

- Collector width (m) ω - exergy efficiency (%) ψ_k Receiver efficiency ((%))

Subscripts and Superscripts

Base fluid bf hnf Hybrid nanofluid Inlet i

k Element *k*, component *k*

Outlet j

Abbreviations and Acronyms

Aluminium dioxide

 Al_2O_3 C Carbon CHP Combined heat and power **CMP** Compressor

Carbon dioxide CO_2 Condenser CON

COP Coefficient of performance **CSP** Concentrated Solar Power

Engineering Equation Solver

EVP Evaporator

EES

FVI Fuel Index Values (FVI) **GCV** Gross Calorific Values

Η Hydrogen HEX Heat exchanger Kalina cycle KC

Levelized cost of energy **LCOE** LiBr Lithium Bromide water MC Moisture Content

MWCNT Multi-walled carbon nanotube

N Nitrogen

NASA National Aeronautics and Space Administration

 NH_3 Ammonia

AUTHORSHIP CONTRIBUTIONS

Authors equally contributed to this work.

DATA AVAILABILITY STATEMENT

The authors confirm that the data that supports the findings of this study are available within the article. Raw data that support the finding of this study are available from the corresponding author, upon reasonable request.

CONFLICT OF INTEREST

The author declared no potential conflicts of interest with respect to the research, authorship, and/or publication of this article.

ETHICS

There are no ethical issues with the publication of this manuscript.

STATEMENT ON THE USE OF ARTIFICIAL **INTELLIGENCE**

Artificial intelligence was not used in the preparation of the article.

REFERENCES

- Mohseni M, Hajinezhad A, Moosavian SF. Thermodynamic analysis and multi-objective optimization of an ORC-based solar-natural gas driven trigeneration system for a residential area. Case Stud Therm Eng 2024;59:104513. [CrossRef]
- Rathore A, Almas, Sundaram S. Energy, exergy and performance analysis of a 380 kWP rooftop PV plant assisted with data-driven models for energy generation. J Therm Eng 2024:1164–1183. [CrossRef]
- Altayib K, Dincer I. Development of a largescale integrated solar-biomass thermal facility for green production of useful outputs. Energy 2024;313:133741. [CrossRef]

- [4] Sharifishourabi M, Dincer I, Mohany A. Modelling of an advanced renewable energy system coupled with hydrogen production and liquefaction for sustainable communities. Energy Rep 2024;12:3386–3404. [CrossRef]
- [5] Nassar Y, Irhouma M, Salem M, El-Khozondar H, Suliman S, Elmnifi M, Khaleel M, Rekik S. Towards green economy: Case of electricity generation sector in Libya. Sol Energy Sustain Dev 2025;14:334–360.
 [CrossRef]
- [6] Nassar YF, El-Khozondar HJ, Fakher MA. The role of hybrid renewable energy systems in covering power shortages in public electricity grid: An economic, environmental and technical optimization analysis. J Energy Storage 2025;108:115224. [CrossRef]
- [7] Ismail MM, Dincer I, Bicer Y, Saghir MZ. Assessment of a solar-powered trigeneration plant integrated with thermal energy storage using phase change materials. Process Saf Environ Prot 2024;191:1339–1352. [CrossRef]
- [8] Liang X, Li Z, Dong H, Ye G. A review on the characteristics of wood biomass fly ash and their influences on the valorization in cementitious materials. J Build Eng 2024;97:110927. [CrossRef]
- [9] Kızgut S, Bilen M, Toroğlu İ, Barış K. Size-related evaluation of unburned carbon. Combust Sci Technol 2016;188:439–450. [CrossRef]
- [10] Toroglu I. Investigation of briquetting of Armutçuk and Amasra coals and investigation of combusting properties of the briquettes obtained. J Ore Dress 2002;4:10–19.
- [11] Sutcu H, Toroglu I, Piskin S. Structural characterization of oil component of high temperature pyrolysis tars. Energy Sources 2005;27:521–534. [CrossRef]
- [12] Su O, Toroglu I, Akcin NA. An evaluation of the impact strength index as a criterion of grindability. Energy Sources A Recover Util Environ Eff 2010;32:1671–1678. [CrossRef]
- [13] Akkaya B, Toroğlu İ, Bilen M. Studying the effect of different operation parameters on the grinding energy efficiency in laboratory stirred mill. Adv Powder Technol 2020;31:4517–4525. [CrossRef]
- [14] Elmaihy A, Rashad A, Elweteedy A, Nessim W. Energy and exergy analyses for organic Rankine cycle driven by cooling water of passenger car engine using sixteen working fluids. Energy Convers Manag X 2023;20:100415. [CrossRef]
- [15] Kara O. An evaluation of a new solar-assisted and ground-cooled organic Rankine cycle (ORC) with a recuperator. Arab J Sci Eng 2023;48:11781–11800.
- [16] Nassar YF, El-Khozondar HJ, Ahmed AA, Alsharif A, Khaleel MM, El-Khozondar RJ. A new design for a built-in hybrid energy system, parabolic dish solar concentrator and bioenergy (PDSC/BG): A case study Libya. J Clean Prod 2024;441:140944. [CrossRef]

- [17] Nassar YF, Abdunnabi MJ, Sbeta MN, Hafez AA, Amer KA, Ahmed AY, et al. Dynamic analysis and sizing optimization of a pumped hydroelectric storage-integrated hybrid PV/Wind system: A case study. Energy Convers Manag 2021;229:113744. [CrossRef]
- [18] El-Khozondar HJ, El-Batta F, El-Khozondar RJ, Nassar Y, Alramlawi M, Alsadi S. Standalone hybrid PV/wind/diesel-electric generator system for a COVID-19 quarantine center. Environ Prog Sustain Energy 2023;42:e14049. [CrossRef]
- [19] Ali AFM, Karram EMH, Nassar YF, Hafez AA. Reliable and economic isolated renewable hybrid power system with pumped hydropower storage. Proc Int Middle East Power Syst Conf 2021:515–520. [CrossRef]
- [20] Nassar Y, Mangir I, Hafez A, El-Khozondar H, Salem M, Awad H. Feasibility of innovative topography-based hybrid renewable electrical power system: A case study. Cleaner Eng Technol 2023;14:100650.
 [CrossRef]
- [21] Salim E, Abubaker A, Ahmed B, Nassar Y. A brief overview of hybrid renewable energy systems and analysis of integration of isolated hybrid PV solar system with pumped hydropower storage for Brack city Libya. West Afr J Pure Appl Sci 2025;3:152–167. [CrossRef]
- [22] Khaleel M, Yusupov Z, Güneşer M, Nassar Y, El-Khozondar H, Ahmed AA, et al. Towards hydrogen sector investments for achieving sustainable electricity generation. Sol Energy Sustain Dev 2024;13:71–96. [CrossRef]
- [23] Sun W, Li T, Hong Y, Chu H, Liu J, Feng L. Dualobjective optimization of biofuel-based solid oxide fuel cell energy system for hydrogen fuel and desalinated water production. Fuel 2023;334:126598. [CrossRef]
- [24] Zhong Z, Zhu J, Li N, Liu W, Gao L, Gao X, et al. Energy, exergy, exergoeconomic, and environmental (4E) analyses of a combined system comprising reformed methanol high-temperature proton exchange membrane fuel cells and absorption refrigeration cycle. Energy Sources A Recover Util Environ Eff 2024;46:16642–16656. [CrossRef]
- [25] Abdoos B, Pourfayaz F, Ahmadi MH, Gholami A. Energetic/exergetic parametric study of a combined cooling, heating, and power (CCHP) system coupled with a local cellulosic biomass combustion chamber. Energy Rep 2024;12:3770–3777. [CrossRef]
- [26] Khoshgoftar Manesh MH, Davadgaran S, Mousavi Rabeti SA, Blanco-Marigorta AM. Feasibility study of green ammonia and electricity production via an innovative wind-solar-biomass polygeneration system. Appl Energy 2025;384:125467. [CrossRef]
- [27] Siddiqui MA, Alsaduni I. Performance assessment of solar tower collector-based integrated system for the cogeneration of power and cooling. Heliyon 2024;10:e39993. [CrossRef]

- [28] Yousef MS, Santana D. Optimizing power, cooling, and hydrogen generation: A thermodynamic and exergoeconomic study of an advanced sCO2 trigeneration system. Case Stud Therm Eng 2024;53:103902. [CrossRef]
- [29] Yilmaz F, Ozturk M, Selbas R. Investigation of the thermodynamic analysis of solar energy-based multigeneration plant for sustainable multigeneration. Sustain Energy Technol Assess 2022;53:102461. [CrossRef]
- [30] Yilmaz F, Ozturk M. Modelling and parametric analysis of a new combined geothermal plant with hydrogen generation and compression for multigeneration. Int J Hydrogen Energy 2023;48:39197–39215. [CrossRef]
- [31] Soyturk G. Design and thermodynamic analysis of sustainable hybrid system based on solar tower and helium gas cycle for green hydrogen and ammonia production. Sustain Energy Technol Assess 2024;72:104077. [CrossRef]
- [32] Boukelia TE, Bessaïh R, Laouafi A. A novel concentrating solar power plant design for power, cooling, and hydrogen production through integrated waste heat recovery system. Int J Hydrogen Energy 2025;106:295–304. [CrossRef]
- [33] Hussein ESH, Mirzaee I, Rash-Ahmadi S, Khalilian M. Thermodynamic and thermoeconomic aspects of utilizing two distinct solar collectors in a multigeneration system. Int J Thermofluids 2025;27:101182.
- [34] Chandio MW, Kumar L, Memon AG, Awad MM. Thermodynamic, economic, and environmental evaluation of internal combustion engine exhaust gas-driven organic Rankine cycles for power generation and desalination. Int J Thermofluids 2025;25:101046. [CrossRef]
- [35] Klein SA. Engineering equation solver (EES). fchart-com/ees 2013. Available at: https://fchartsoftware.com/ees/ Accessed on Nov 18, 2025.

- [36] Rajput RK. Thermal engineering. 9th ed. New Delhi (India): Laxmi Publications Ltd; 2014.
- [37] Kalogirou SA. Solar thermal collectors and applications. Prog Energy Combust Sci 2004;30:231–295.

 [CrossRef]
- [38] Tyagi SK, Wang S, Singhal MK, Kaushik SC, Park SR. Exergy analysis and parametric study of concentrating type solar collectors. Int J Therm Sci 2007;46:1304–1310. [CrossRef]
- [39] Akhator P, Asibor J, Obanor A. Chemical composition and combustion properties of tropical wood species from Nigeria. Niger J Eng 2022;29.
- [40] Bejan A, Tsatsaronis G. Thermal design and optimisation. New York: John Wiley and Sons Inc; 1995.
- [41] Takabi B, Salehi S. Augmentation of the heat transfer performance of a sinusoidal corrugated enclosure by employing hybrid nanofluid. Adv Mech Eng 2014;2014:147059. [CrossRef]
- [42] Parikhani T, Gholizadeh T, Ghaebi H, Sadat SM, Sarabi M. Exergoeconomic optimization of a novel multigeneration system driven by geothermal heat source and liquefied natural gas cold energy recovery. J Clean Prod 2018;209:550–571. [CrossRef]
- [43] Ozturk M, Dincer I. Thermodynamic analysis of a solar-based multigeneration system with hydrogen production. Appl Therm Eng 2013;51:1235–1244.
- [44] Karaca AE, Dincer I. A new integrated solar energy based system for residential houses. Energy Convers Manag 2020;221:113112. [CrossRef]
- [45] Khanmohammadi S, Heidarnejad P, Javani N, Ganjehsarabi H. Exergoeconomic analysis and multi-objective optimization of a solar-based integrated energy system for hydrogen production. Int J Hydrogen Energy 2017;42:21443–21453.